JOURNAL OF MATERIALS SCIENCE 31 (1996) 6583–6594

Fracture mechanisms of the *Strombus gigas* conch shell: implications for the design of brittle laminates

L. T. KUHN-SPEARING*, H. KESSLER, E. CHATEAU, R. BALLARINI‡, A.H. HEUER
Department of Materials Science & Engineering, and ‡Department of Civil Engineering, Case Western Reserve University, 10900 Euclid Avenue, Cleveland, OH 44106, USA

S. M. SPEARING
Department of Aeronautics and Astronautics, Massachusetts Institute of Technology, 77 Massachusetts Avenue, Cambridge, MA 02139, USA

Flexural strength, crack-density evolution, work of fracture, and critical strain energy release rates were measured for wet and dry specimens of the *Strombus gigas* conch shell. This shell has a crossed-lamellar microarchitecture, which is layered at five distinct length scales and can be considered a form of ceramic "plywood". The shell has a particularly high ceramic (mineral) content (99.9 wt%), yet achieves unusually good mechanical performance. Even though the strengths are modest (of the order 100 MPa), the laminated structure has a large strain to fracture, and a correspondingly large work of fracture, up to 13 kJ m^{-2}. The large fracture resistance is correlated to the extensive microcracking that occurs along the numerous interfaces within the shell microstructure. Implications of this impressive work of fracture for design of brittle laminates are considered.

1. Introduction

Mollusc shells can be described in terms used for advanced structural materials: they are high-toughness, intermediate-strength, ceramic (mineral)/polymer (protein) laminated composites. These biologically produced materials are composed of aligned, anisometric, calcium carbonate ($CaCO_3$) grains [1–4] separated by extremely thin organic (proteinaceous) layers [5]. The $CaCO_3$ grains are laminated in layers at multiple length scales, with a periodicity and self-similar architecture not yet duplicated by synthetic processing. The microstructure plays a key role in enhancing the toughness, strength, and hardness of the shell by constraining crack growth and delocalizing deformation [6–8]. During previous mechanical property studies, a three-orders-of-magnitude increase in toughness [7], and a two-fold increase in hardness of shell $CaCO_3$ over that of non-biogenic $CaCO_3$, was measured [1, 3]. Extensive crack deflection at mineral/organic interfaces at several length scales was observed [7]. These observations of the fracture mechanisms in seashells may have inspired material scientists to produce layered synthetic materials with controlled interfacial properties that also encourage crack deflection and multiple cracking [9–13]. However, the level of delocalized cracking achieved in ceramic composities has not yet matched that observed in biologically produced materials, suggesting that additional design strategies for synthetic materials remain to be discovered.

To understand better the design of mollusc shells, we have conducted experiments and applied analyses developed for the fracture of composite laminates to the *Strombus gigas* conch shell. Conchs are active burrowers, and require a hard, abrasion-resistant shell. The great mass of the shell provides stability against upheaval by tidal forces or predatory attackers, as well as protection from crab attacks that may involve forces as great as 800 N [14]. The microstructure that naturally evolved to suit this lifestyle is known as the crossed-lamellar microstructure and consists of lath-like aragonite crystals separated by a tenuous organic layer (the total organic content is $\sim 0.1\%$ by weight). In section it is reminiscent of plywood or crossed-ply fibre-reinforced laminated composites, with the macroscopic layers of the structure playing the role of the plies of a synthetic composite. In addition to flexural strength, crack-density evolution measurements and modelling, and work of fracture determination, we applied the methods used

**Present address*: Laboratory for the Study of Skeletal Disorders and Rehabilitation, Department of Orthopaedic Surgery, Harvard Medical School, Children's Hospital, 300 Longwood Avenue, Boston, MA 02115, USA.

0022–2461

by Charalambides *et al.* [15] to quantify the interfacial fracture resistance. An advantage of studying the conch shell is that the fine-scale layering is located in more than one plane, allowing two independent interfacial fracture measurements to be made, and also allowing the toughness contributions from the various layers to be separated and identified.

In general, the evolutionary trend in the mollusc family has been toward a reduction of the organic content of the shell and a finer grain size [16]. With 99.9 wt % ceramic (mineral), the crossed-lamellar structure is at the pinnacle of mollusc evolution. While the tensile strengths of crossed-lamellar shell are 50% lower than the strongest shell microstructure (nacre: brick and mortar microstructure: 95% mineral content [16]) we show in this paper that the structural advantage realized in the crossed-lamellar shell is a work of fracture which is nearly ten times higher than that reported for nacre [17]. We conclude with suggestions for the bioinspired (biomimetic) design of tough, damage-tolerant, synthetic layered materials.

2. Experimental procedure

2.1. Materials

Large *Strombus gigas* conch shells of Caribbean origin (25–30 cm maximum dimension) were used for this study (Fig. 1). The shells were received dry with the periostracum (external organic coating) removed by chemical and mechanical methods. 40 bend test specimens were cut from the last whorl of six shells in the two orientations shown in Fig. 1. The majority of the samples (27 of 40) were cut with their long direction parallel to the major axis of the shell (referred to as "parallel" orientation) because of the extensive cracking observed in prior studies of this orientation [6]. It was also easier to obtain uncurved samples with large span to depth ratios in the parallel orientation as compared to the "perpendicular" orientation.

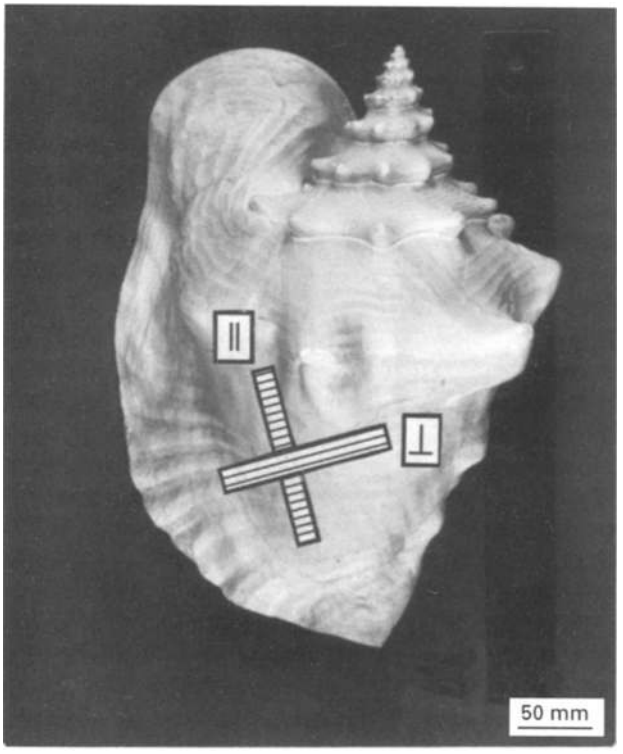

Figure 1 A large (25–30 cm) *Strombus gigas* conch shell from which mechanical test specimens were machined. Two orientations were tested: parallel, ∥, and perpendicular, ⊥ to the shell axis.

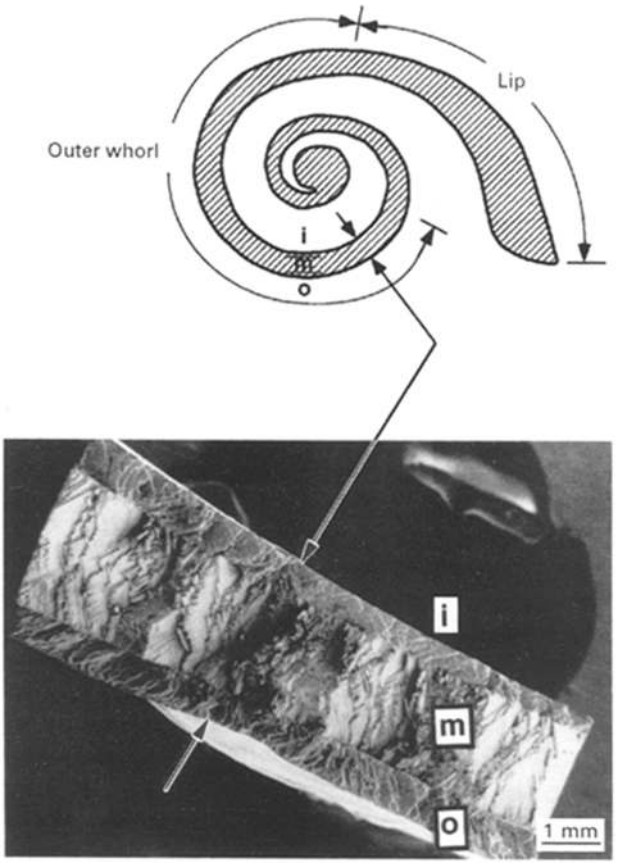

Figure 2 Samples for this study were taken from the outer whorl which has three macroscopic layers: i, inner; m, middle; o, outer. The vulnerable lip area is strengthened by a thickened middle layer. The inner whorls are much thinner due to delibrate dissolution which gives the organism more room inside of the shell.

In the last whorl of the shell, from which the test specimens were cut, there are three macroscopic layers – inner (closet to the organism), middle and outer – which are in a 0°/90°/0° arrangement (Fig. 2) and of a relatively uniform thickness within the last whorl. The outermost edge of the shell (the lip) has a thickened middle layer to enhance the mechanical strength; for consistency, therefore, samples were only taken from the last whorl.

The microstructure within a bend specimen with a parallel orientation is depicted schematically in Fig. 3. Each macroscopic layer is composed of layers of first-order lamellae which are perpendicular to the macroscopic layers and oriented $\pm$ 35°–45° relative to each other. Embedded within each first-order lamella are long thin laths stacked in parallel, which are known as second-order lamellae. The second-order lamellae are polycrystalline, and are composed in turn of single crystal third-order lamellae, each of which is layered at an atomic scale by very-fine growth twins (polysynthetic twins) [3]. The aspartic acid-rich organic matrix (0.1 wt %) has only been observed by TEM as an electron dense layer that envelops each of the third order lamellae [4, 5] ("matrix" is the term

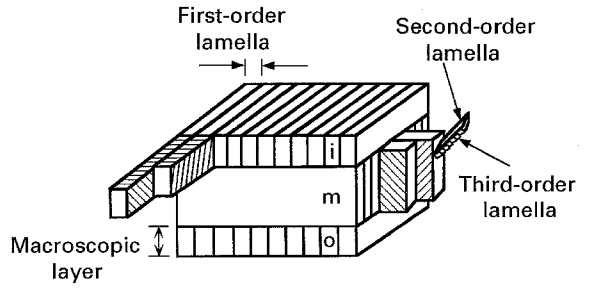

Figure 3 A simplified schematic drawing of the crossed-lamellar structure within a four-point bending specimen in the parallel orientation (not drawn to scale). Each macroscopic layer is composed of first-, second- and third-lamellae and the third-order lamellae are twinned, comprising a total of five different layering schemes in the shell structure.

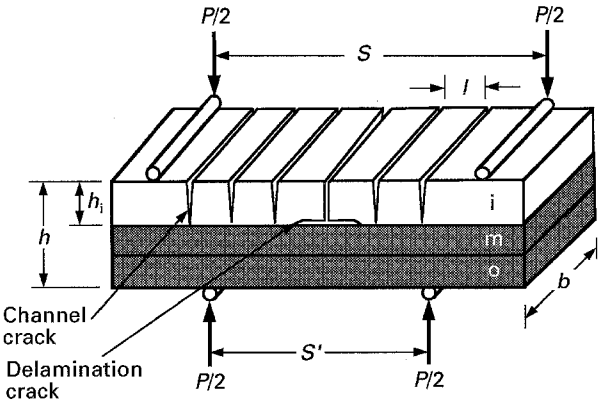

Figure 4 Bend specimen loading configuration, shown relative to the material architecture, with a typical pre-failure cracking pattern (channel and delamination cracks).

used by biologists to refer to the protein portion of the hard (mineralized) tissue). Microscopy studies have not shown the presence of additional organic matrix between the other layers, although we believe organic matrix material does separate adjacent first- and second-order lamellae. More detailed descriptions of the crossed-lamellar structure may be found in Taylor and Layman [1], Kohn *et al.* [2], Laraia and Heuer [3], Wilmot *et al.* [4], and Currey and Kohn [6].

2.2. Test specimens

Preliminary sectioning of the shells was performed with an industrial Felker 41A saw using an 11 in (~ 28 cm) diamond blade. These pieces were embedded in Snow-White impression plaster, which provided support of the irregularly shaped pieces so that they could be cut into beam specimens by a 6 in (~ 15.25 cm) diamond wheel saw blade mounted on a Reid precision surface grinder (Fay Scott model HYD DF). The sides of the specimens were polished using 220 and 600 SiC grit, and 9, 3 and 1 μm diamond abrasives on a Struers Planopol PEDEMAX polishing machine, but the inner and outer surfaces of the shell were left in the as-grown condition to preserve the microstructure for fracture testing and analysis. To obtain wet samples for testing and analysis, cut sections of the dry shell were immersed in artificial sea water (0.1 M NaCl and 0.011 M KCl, pH = 8.5) prior to testing for periods ranging from 3–9 weeks. A light optical microscope was used to measure accurately the macroscopic layer thicknesses.

2.3. Experiments

Displacement-controlled (0.1 mm min^{-1}) four-point bend tests were conducted at room temperature on an Instron 1125 testing machine with a 10 kN load cell and a QuickLog data acquisition package (Strawberry Tree Computers, Inc.). The majority of the samples tested were of the parallel orientation because of the extensive cracking (channel cracks [18]) which occurs in this orientation [6] (cracking patterns are shown in Fig. 4) and because it was difficult to obtain comparably long, uncurved specimens in the perpendicular orientation. To minimize in-plane shearing stresses, the inner and outer load-point locations were selected based on the recommendations of Charalambides *et al.* [15]. The gauge length, S, varied from 35–80 mm, the depth, h, from 2.3–6.3 mm and the width, b, of the specimens from 2.9–13.9 mm (see Fig. 4 for variable definition). On average, the span to depth ratio was 12. The lower load points were supported on a spring-loaded stage that could self-adjust in planes parallel and perpendicular to the loading pins to accommodate the shell surface irregularities. A linear voltage displacement transducer (LVDT) was used to monitor the midpoint deflection, δ, of the tensile surface. The samples were continuously monitored during testing by unaided visual observation with bright lighting, so that the first cracking load, as well as the number of cracks, N_c, between the inner load points could be recorded as a function of load, P. These data were used to generate the crack-density evolutions. Dye penetrant was used after the test to facilitate crack counting. Wet samples that had been reconstituted in artificial sea water were also tested for comparison. The samples were tested immediately after removal from the artificial sea water without drying and without additional application of water during testing. Scanning electron microscopy on a Jeol 35CF at 2 and 25 kV was utilized to characterize the fracture surfaces.

2.4. Analyses

Strength, crack-density evolution and work of fracture were measured for wet and dry specimens of the *Strombus gigas* conch shell as follows. The stress at which first cracking occurred was determined from the standard linear beam bending equation: $\sigma = My/I$, where M is the moment corresponding to the first cracking load, M_c, y is the distance from the neutral axis, and I is the moment of inertia. Flexural strength was calculated from this formula using the moment corresponding to the maximum recorded load and by setting y equal to half the full thickness.

As will be discussed below, the occurrence of multiple cracks at the first-order interfaces is the key to the

damage tolerance of the conch shell; thus channel crack-density evolution was carefully measured. For comparison with the experimental crack-density evolution, a finite element model was implemented to predict crack density, N_c/l, as a function of M/M_c as described in the Appendix. Values for the work of fracture, W_f, which encompasses channel cracking and all additional fracture mechanisms, were obtained by integrating the area under the P–δ curves and normalizing by the cross-sectional area of the samples (bh) [19].

Interfacial toughness estimates were made for two different interfaces: first-order interfaces and the macroscopic interfaces. Application of tensile stresses to the first order interfaces results in *multiple* parallel cracks. Nonetheless, the energy release rate for a first-order interface can be estimated using the traditional compliance change approach for a *single* crack. When a single crack of area A, in a linear elastic material, grows by an amount dA, at load P, the energy to create new crack surface, $\mathcal{G}_c$, can be computed from the resulting compliance change, dC [20]

$$\mathcal{G}_c = \frac{P^2}{2}\frac{\partial C}{\partial A} \tag{1}$$

This expression (which assumes linear elasticity) was used to approximate an average $\mathcal{G}_c^{chan}$ for *multiple* cracks at the first-order interfaces of the conch shell as follows. The compliance as a function of crack number was obtained from tests in which the sample was unloaded and reloaded after visually observed cracking events. A value for the differential compliance change was taken as the slope of a straight line fitted to the compliance as a function of observed crack number. When several channel cracks grew simultaneously, the energy was divided equally between the cracks by approximating the increase of crack area, dA, by $\Delta N h_i b$, where ΔN is the number of newly formed channel cracks, h_i is the thickness of the multiply-cracked inner layer, and b is the width of the beam. Example compliance calculations are included in Section 3.

To evaluate the macroscopic interface fracture resistance, the four-point bend delamination test outlined elsewhere [15, 21] was conducted. During the testing we found that delamination cracking occurs naturally in the conch shell due to the 0°/90°/0° architecture. In the parallel orientation, (channel) cracks initiate between first-order layers and propagate rapidly to the macroscopic layer interface (Fig. 4). They are arrested and redirected along the interlayer interface parallel to the neutral axis of the beam, making it unnecessary to prenotch the samples for the inter-layer fracture resistance tests. An estimate of the fracture resistance, $\mathcal{G}_c^{delam}$, of a delamination crack can be obtained from the formula for a symmetrically cracked beam loaded in four-point flexure [21]

$$\mathcal{G}_c = c_1 P^2 \frac{((S - S')/2)^2 (1 - v^2)}{E b^2 h^3} \tag{2}$$

The constant c_1 is a function of the elastic modulus ratio and the cracked/uncracked layer thickness ratio and can be determined from the numerical results presented in Ref. [21]. For the dimensions of the samples in this study, and based on the assumption of equal modulus for the macroscopic layers, c_1 is 10 or 10.5 for the conch shell specimens we tested. P is the constant load observed during steady-state delamination cracking, v is Poisson's ratio, E is Young's modulus, and h is the total thickness. A modulus of 60 GPa was assumed, based on averaging published data for shells [22]. In the absence of any data available for Poisson's ratio, a value of 0.3 was used.

3. Results

3.1. Failure in the parallel orientation

During fracture of the crossed-lamellar material, cracks are forced to follow a tortuous path along the ceramic/protein interfaces, as seen in the fracture surface of a parallel sample in Fig. 5a. During bending with the inner layer in tension, the main crack initiates on the inner layer (i) surface, and eventually propagates through the three layers. Cracks temporarily arrest at the inner/middle interface due to the 90° layer rotation, and are then directed at $\pm$ 45° through the middle layer by second-order interfaces. The first-order interfaces are relatively smooth, although lamellae that may have bridged the crack before failure are visible in Fig. 5b. The crack also steps between second-order interfaces, and at increased magnification (Fig. 5c), it can be seen that the crack is being deflected along the third-order interfaces (Fig. 5d). Cracks propagate along the first-, second-, and third-order organic lamellar boundaries, rather than within the aragonite crystallites.

Representative load–deflection (P–δ) data from four-point bend tests of parallel orientation dry and wet crossed-lamellar samples are shown in Fig. 6 (inner layer in tension). Initial elastic behaviour became non-linear and included small load drops followed by load increase, before the peak load was reached. In the parallel orientation, the interfaces between the first-order lamellae of the macroscopic inner layer are in tension. Multiple channel cracks formed in the inner layer under increasing load and were visually correlated to the small load drops that appeared with increasing strain (Fig. 6). Often more than one crack occurred per load drop. Such cracks were arrested at the inner/middle interface due to the different orientation of the middle layer. The channel cracks (enhanced by dye penetrant) are visible in the optical micrograph of a fractured remnant of a bend specimen (Fig. 7). Usually some slight delamination was associated with the intersection of the crack at the middle/inner interface. Additional inner layer cracks initiated below the tensile surface, within the inner layer or at the interface with the middle layer, rather than at the tensile surface, as can be seen arrowed in Fig. 7.

Eventually failure occurred when a single crack penetrated through both the middle and outer layers (Fig. 8a). The outer layer has the same microstructural orientation as the inner layer and offers little resistance to crack propagation. Examples of "graceful" failure observed in six of the dry samples and three of the wet samples tested in the parallel orientation are

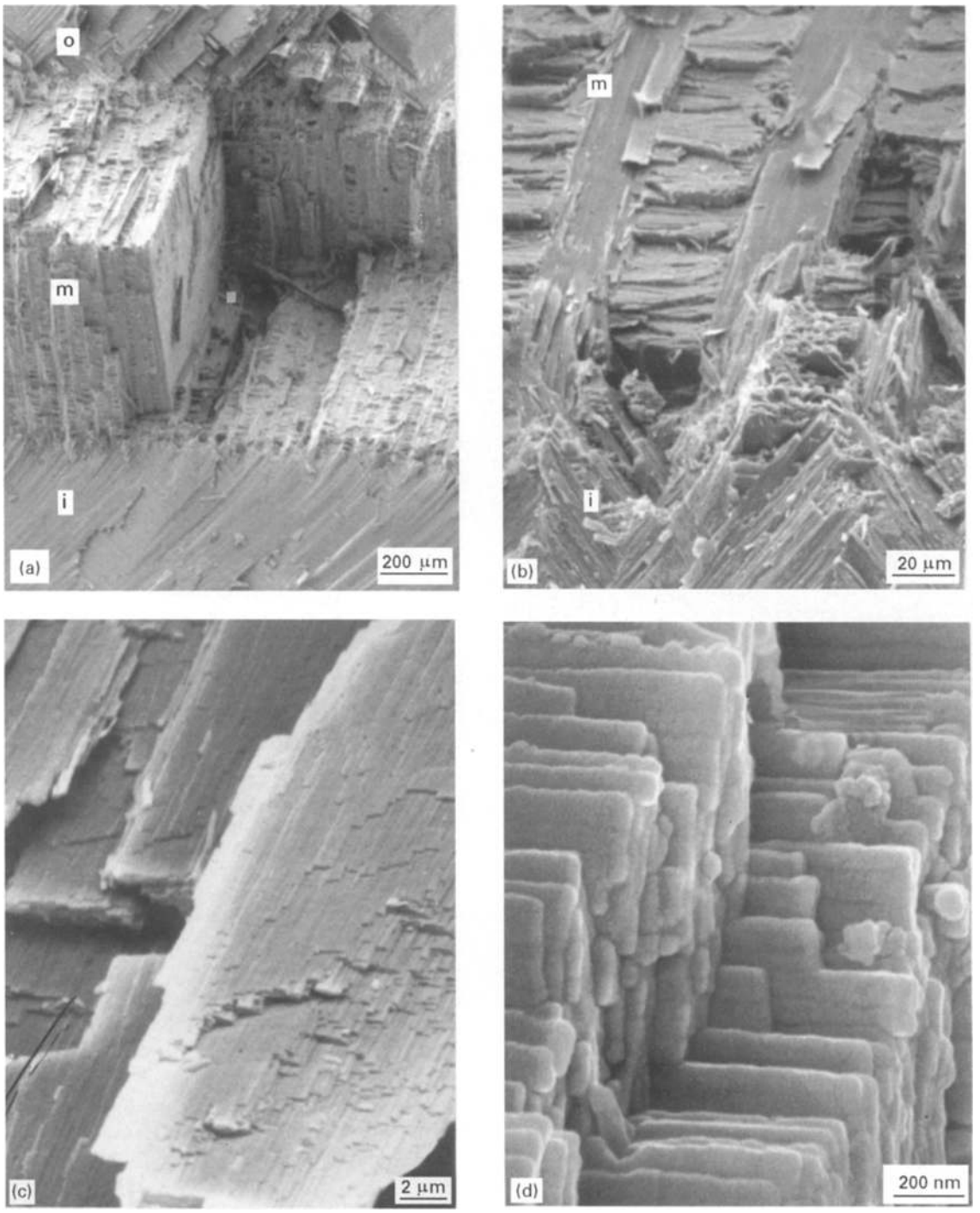

Figure 5 A fracture surface from a four-point bend specimen, showing extensive delocalized, interfacial cracking. (a)–(d) show the fracture surface at increasing magnification. In (a) the crack propagated from the inner layer to the outer layer (bottom to top), arresting temporarily at the inner/middle interface due to the change in microstructural orientation ("orientation toughening"). The first-order interfaces that appear smooth in (a), appear "woody" at higher magnification (b). In (c), the crack path within the second-order lamellae is directed along interfaces between third-order lamellae shown in (d).

shown in Fig. 8a and b. The bend fragments are held together by frictional interference of bridging first- and second-order lamellae in the middle layer (Fig. 8a and b). Note the interlayer delamination cracking, at the inner/middle macroscopic layer interface (Fig. 8b) which occurred in nine of the 40 samples tested.

3.2 Channel cracks and failure in the perpendicular orientation

First channel cracking occurred at an average stress of 35 ± 17 MPa for seven dry samples, and at much lower stresses for wet samples, reflecting the reduction in strength of the organic component when wet. (Actual values for wet samples and several of the dry samples were not recorded because channel cracks were introduced before beginning the test by the small loads used for sample alignment.) Presumably, the flexural strength is governed by the strength of the largely uncracked middle layer. However, there is considerable uncertainty associated with calculating the stress on this layer, and thus the flexural strengths were calculated based on standard linear beam-bending equations using the average full-beam thickness.

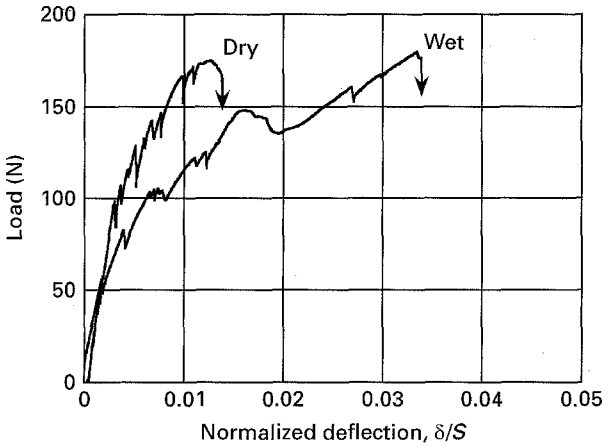

Figure 6 Representative load (P)–deflection (δ) curves for wet and dry conch specimens tested in the parallel orientation. The characteristic load drops represent inner layer and delamination cracking.

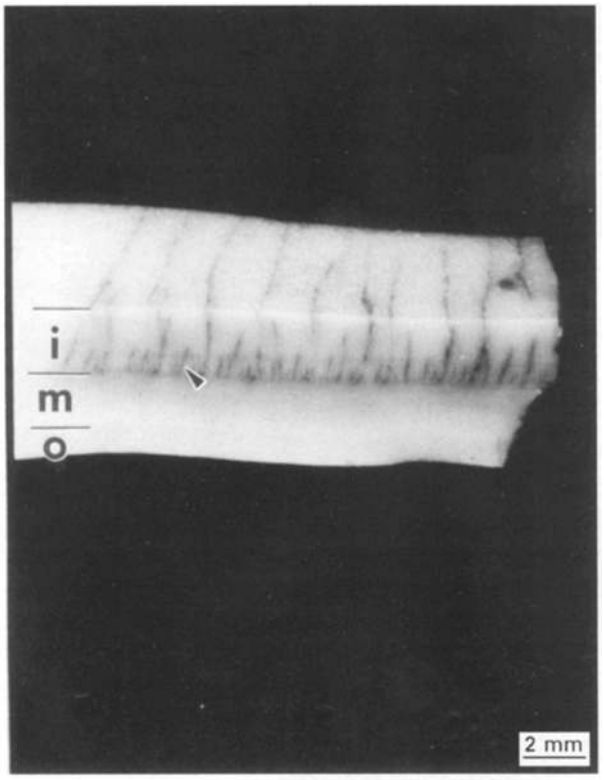

Figure 7 An optical micrograph of one-half of a bend specimen with a dye penetrant-enhanced crack pattern. The arrow points to secondary channel cracks believed to initiate below the surface within the interface, after the primary cracks have formed and released the stress on the surface.

The average apparent flexural strengths for the dry and wet crossed-lamellar samples in the parallel orientation are 56 ± 22 MPa (13 samples) and 84 ± 49 MPa (9 samples), respectively. {Currey and Kohn [6] calculated shell strengths using the middle and outer layer thickness only, based on the assumption that the inner layer did not contribute to the strength. Our calculations of the strength based on an uncracked thickness give values with relatively less deviation: 182 ± 71 MPa and 215 ± 71 MPa, implying there is a relationship between strength and relative inner layer thickness. However, insufficient

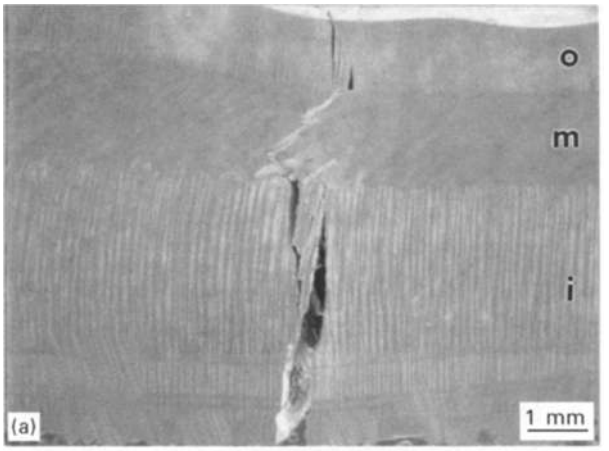

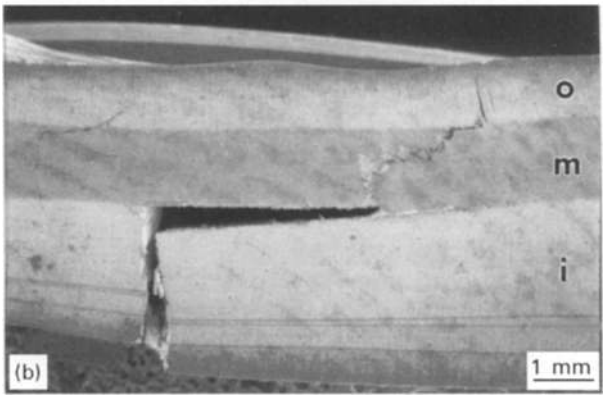

Figure 8 Side view of two fractured samples (parallel orientation); (a) a dry specimen with no delamination, but with first-order crack bridging; (b) a wet specimen with delamination along macroscopic layer interfaces. The striped vertical contrast visible in the inner and outer layers in (a) highlights alternating first-order lamellae, and originates from small height differences that arise during polishing due to hardness anisotropy within the material ("relief polishing").

samples were tested with varying inner layer thicknesses to determine this relationship quantitatively.} Additional uncertainties are associated with these estimates due to the non-linearity of the $P - \delta$ response (approximately + 15% [23]) and natural shell irregularities. The average apparent flexural strength of the perpendicular wet and dry samples was 107 ± 38 MPa (two wet samples and two dry). In the perpendicular orientation, the first-order interfaces of the inner layer are parallel to the direction of loading, and channel cracks cannot initiate and weaken the inner layer supporting the highest tensile stresses.

Representative channel crack densities are plotted in Fig. 9a as a function of normalized bending moment. The applied bending moment, M, is divided by the moment at first channel cracking, M_c; where M_c could not be measured directly, the crack density versus stress curve was fitted and extrapolated to zero load to infer a value for M_c. The data points are from individual tests and the shaded areas define the boundaries of the data for dry and wet shell samples. The crack density, $1/l$, where l is the spacing between channel cracks, is normalized by the uncracked thickness ($h - h_i$) measured by light optical microscopy. The dry shells fail at lower M/M_c ratios, with lower final crack densities, than do the wet shells (Fig 9a). Saturation crack densities were not observed for either

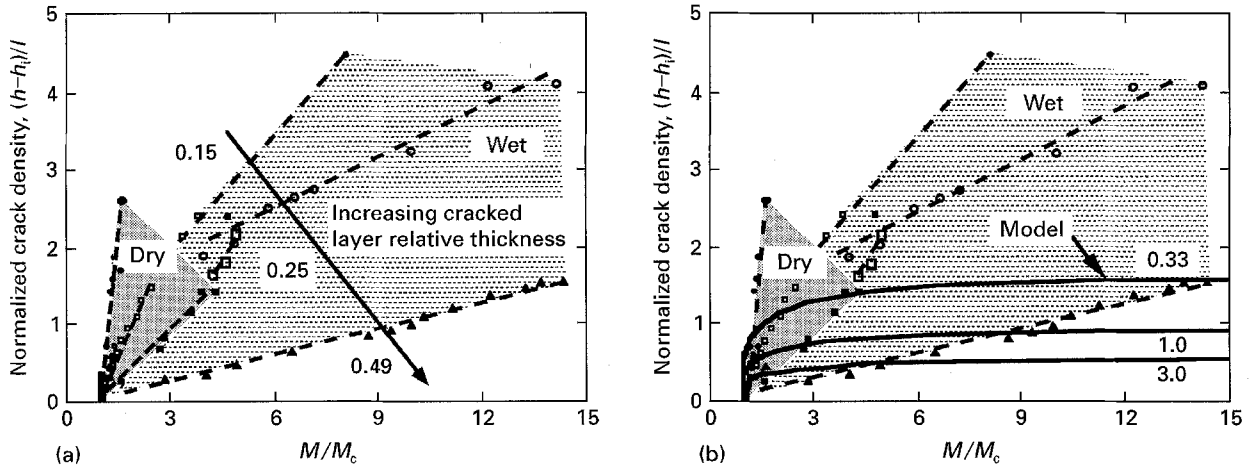

Figure 9 Normalized crack density ($(h - h_i)/l$) versus normalized bending moment M/M_c; M_c is the moment at first channel cracking. The shaded and stippled areas in (a) and (b) define the range of the data for dry and wet shells, respectively. A higher crack density is observed for samples that have a thinner cracked layer (the cracked/uncracked ratios; (●) 0.15, (□) 0.25, (▲) 0.49. (b) The same data, along with the stress-based model predictions generated from finite element analysis (—) for three relative thicknesses of cracked layer. The model predicts the experimentally observed sensitivity to relative layer thickness, although the predicted saturation crack density is not in agreement with experiment.

wet or dry shells. Higher final crack densities were observed in both dry and wet shell samples with a relatively thin cracked layer relative thickness.

The model for channel crack evolution as a function of applied bending moment described in the Appendix is compared to the data in Fig. 9b. The criterion used in the simulation is strength-based, with new crack initiation based on the stress at the tensile surface of the finite element specimen. The strength-based or initiation-controlled model predicts that crack density will increase as the cracked/uncracked thickness ratio decreases, $h_i/(h - h_i)$, which is in broad agreement with the data (Fig. 9b). In samples with a relatively thin inner layer, less stress is relieved in the outermost cracked regions by neighbouring cracks, allowing additional crack initiation on the tensile surface. The model also predicts a saturation crack density, which was not observed.

3.3. Work of fracture

The total energy associated with the numerous cracking events during fracture of the conch shell can be approximated by the work of fracture, W_f. Considering the large extent of delocalized cracking seen during fractographic examination, it is not surprising that high toughness values were obtained: $4 \pm 2\,kJ\,m^{-2}$ for 11 dry shell specimens and $13 \pm 7\,kJ\,m^{-2}$ for eight wet shell specimens tested in the parallel orientation. Recall that in the wet samples, more extensive damage was observed: a higher channel crack density, additional delamination at the inner/middle interface, and multiple middle layer cracks penetrating partially through the middle layer thickness, all of which contribute to W_f.

Table I lists the W_f values and the associated span to depth ratio and a mircoarchitectural dimension (percentage of inner layer). There are insufficient data to draw statistical correlations; however, in general,

TABLE I W_f for parallel samples (inner layer in tension)

Dry			Wet		
W_f	S/h	% inner	W_f	S/h	% inner
5.2	10.3	42	15.2	12.5	15
1.6	12	44	13.1	11.8	9
1.2	11.2	43	15.3	12.5	25
7.2	12.3	48	7.7	11.1	28
2.9	14.7	48	4.4	8.6	61
5.6	17.2	51	13.6	12.5	47
3.1	11.6	39	12.3	10.4	49
3.2	11.6	46	6.0	13.8	52
5.1	7.9	58			
2.5	13.5	45			
5.0	21.7	15			

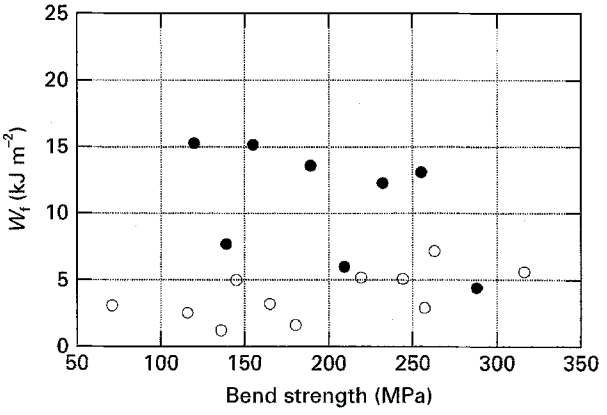

Figure 10 Work of fracture, W_f, versus the bend strength, σ_b. Note that W_f remains relatively constant, even though the bend strength varies between shell samples. (○) Dry (parallel), (●) wet (parallel).

the W_f values were roughly constant for all S/h and per cent inner values tested.

As seen in Fig. 10, the shell structure appears to be designed such that variations in the flexural strength do not greatly affect the overall work of fracture. Although the flexural strength varies among shells by

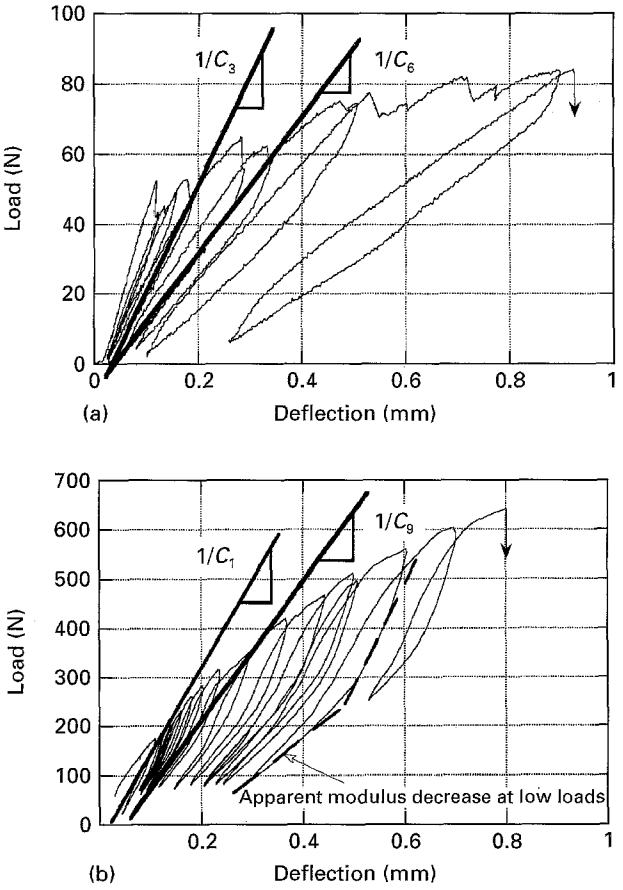

Figure 11 Load (P)–deflection (δ) curves in four-point bending for conch shells. Non-linear, permanent deformation and hysteresis is evident in the unloading/reloading cycles: (a) dry, and (b) wet. The compliance subsequently used for the calculation of channel crack, $\mathcal{G}_c$, was determined from lines drawn through the loading/unloading data, as shown.

a factor of 5, the W_f is relatively constant within the bounds of the data.

3.4. Interfacial toughness measurements

3.4.1. First-order interfaces, $\mathcal{G}_c^{chan}$

Apart from the limited low-load elastic response of the shell, the P–δ curve is non-linear (Fig. 11a), due to microcracking between first-, second-, and third-order lamellae, and delamination between macroscopic layers. Unloading after limited crack propagation revealed permanent deformation, hysteresis which increased with increasing load, and an apparent decrease in modulus at low loads (Fig. 11a and b). Similar behaviour for nacre was reported by Taylor and Layman [1]. The lower initial modulus is related to the reduced compliance of the cracked material, while the hysteresis and permanent deformation are consistent with frictional sliding between pulled-out lamellae bridging cracks.

The complicated loading/unloading behaviour of the crossed-lamellar structure, and permanent plastic deformation, introduce large uncertainties in compliance evaluation, and hence $\mathcal{G}_c^{chan}$ for the first-order interfaces. In this analysis, the inverse slope of a line drawn between the intersection of the load drop line and the reloading data line, and the approximate

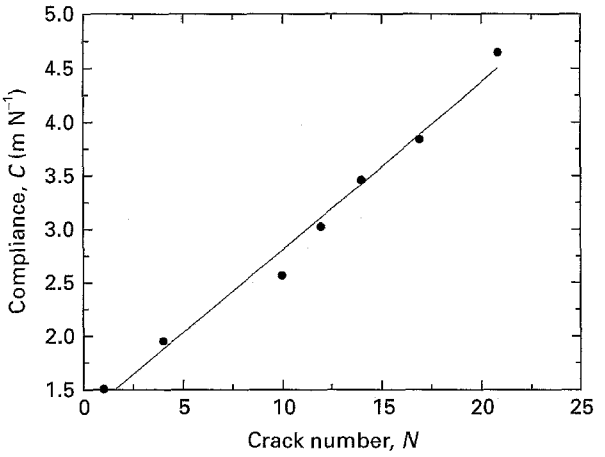

Figure 12 Compliance (from Fig. 11) as a function of crack evolution. The compliance increases as a function of channel crack number, N. A linear fit was used to calculate $\mathcal{G}_c^{chan}$.

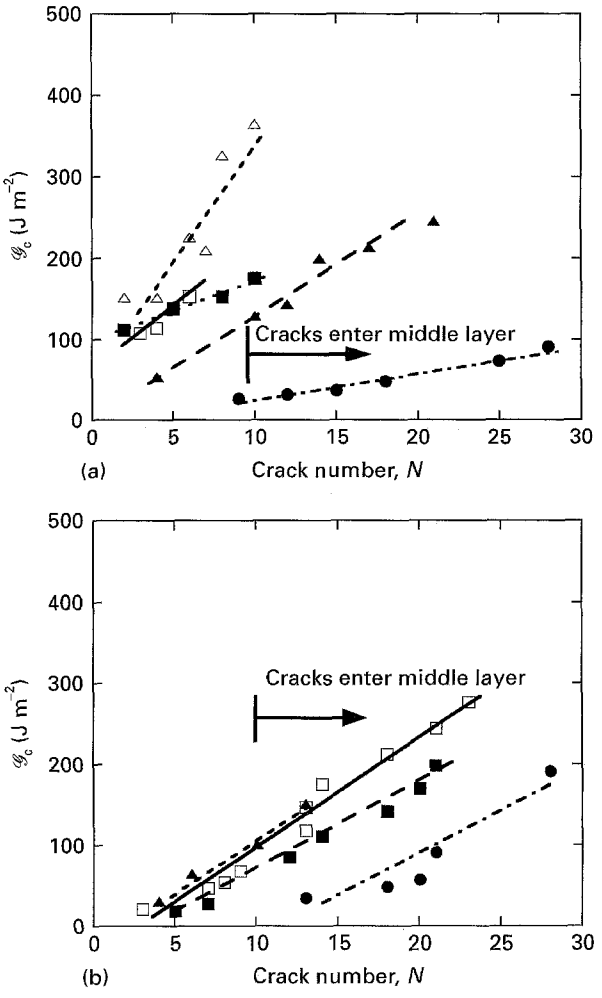

Figure 13 Channel crack $\mathcal{G}_c^{chan}$, as a function of channel crack number, N, for (a) dry and (b) wet shells. The initial values of $\mathcal{G}_c^{chan}$ more accurately reflect the true energy release rate of a channel crack, because at higher crack numbers, the calculation includes those cracks that have entered the apparently higher $\mathcal{G}_c$ middle layer. Sample: (●) 1, (□) 2, (▲) 3, (■) 4, (△) 5.

point of permanent deformation was taken as the compliance (Fig. 11a and b). An example of the data and linear fit used to compute the differential compliance change is shown in Fig. 12.

As shown in Fig. 13a and b for the five dry and four wet samples analysed, there is an apparent systematic

increase of channel crack, $\mathcal{G}_c^{chan}$, with crack number for a given sample, in both dry and wet shells. The initial average values of $85 \pm 46\,J\,m^{-2}$ (dry) and $25 \pm 7\,J\,m^{-2}$ (wet) increase by as much as a factor of 4. The channel crack energy release rate, $\mathcal{G}_c^{chan}$, obtained by averaging over all crack numbers, is $144 \pm 84\,J\,m^{-2}$ for dry shell, and $111 \pm 74\,J\,m^{-2}$ for wet shell, which is similar to that for brittle expoxy. The calculation included the data at loads near failure, when it was observed that more than one crack had penetrated into the more crack-resistant middle layer.

3.4.2. Macroscopic layer interfaces, $\mathcal{G}_c^{delam}$

As seen in Fig. 8b, delamination cracking along the interface between the inner and middle layers is an additional mechanism of delocalized cracking utilized by the crossed-lamellar structure during fracture. Substitution of the measured values into Equation 2 gives an estimate of $\mathcal{G}_c^{delam}$ for dry shell of $106 \pm 29\,J\,m^{-2}$ (four samples). For shells immersed in artificial sea water for two months, the estimates were slightly lower: $73 \pm 36\,J\,m^{-2}$ (five samples). However, this decrease is somewhat misleading. During fracture testing, delamination cracking usually followed some initial channel cracking. At each channel crack tip, superficial localized delamination cracking was observed that served to precrack the interface prior to propagation of the macroscopic delamination. The apparent delamination, $\mathcal{G}_c^{delam}$, for wet shells thus appears lower.

4. Discussion

4.1. Channel cracks

We hypothesized that the multiple cracking between first-order layers was important to the damage tolerance of the conch shell and hence measured and theoretically generated the crack-density evolution. However, we found that, in general, the model based on a simplified material architecture underestimates the relative crack densities that are achieved. This is likely due to the experimentally observed crack bridging by irregular first-order lamellae that deviate from the ideal 0° orientation. Furthermore, first-order lamellae do not completely traverse the bend specimen as they have varying dimensions [6]; this is not shown in the simplified schematic drawing of Fig. 3. Bridging lamellae could support additional channel crack initiation by transferring stress across the crack opening, and thus permit a higher stress in the cracked layer. This implies that use of precisely laminated 0°/90°/0° designs, which encourages the multiple channel cracking by causing crack arrest, can be improved by including some layers with irregular geometry. In addition, some of the cracks do not initiate at the tensile surface (recall Fig. 7b) but were included in our measurements. Note that the wet samples, which have higher flexural strengths, appear to be approaching a saturation crack density (Fig. 9b), implying that a relatively low flexural strength inhibits saturation crack development.

4.2. Work of fracture

The work of fracture measured here is higher than the values reported for nacreous shells (dry $0.4\,kJ\,m^{-2}$ and wet $1.8\,kJ\,m^{-2}$ [17]), several thousands times higher than that of pure aragonite ($0.6 \times 10^{-3}\,kJ\,m^{-2}$ [17]), and comparable to that of antler (wet $13.3\,kJ\,m^{-2}$ [17]). These impressive values appear to be primarily due to the extremely tortuous path of the crack through the crossed-lamellar structure, combined with frictional dissipation between fractured lamellae. The fractographs in Figs 5 and 8 indicate that layers of at least four length scales are involved in the fracture process: macroscopic layers (delamination cracking), first-order layers (channel cracks), second-order layers (middle layer cracks), and third-order lamellae (visible, but not quantified in this study). A bio-inspired design would, therefore, include layering schemes at three to four length scales.

4.3. Interfacial toughness measurements

4.3.1. First-order interfaces

The increase of first-order interfacial $\mathcal{G}_c^{chan}$ with crack number observed in Fig. 13a and b most probably reflects a higher $\mathcal{G}_c$ value for cracks propagating in the middle layer, rather than variable interphase properties in the first-order interfaces. Therefore, we give greater credence to the initial (low load) estimates of $\mathcal{G}_c^{chan}$.

Jackson *et al.* [7] proposed that the increased work of fracture for wet nacre was due to increased plastic deformation of the proteinaceous material at the interface. In the crossed-lamellar structure, which contains a much lower volume fraction of proteinaceous material (0.1% versus 3.0% in nacre), we observed a lower $\mathcal{G}_c$ for wet samples, which is not consistent with increased plastic deformation. Hence a different fracture resistance mechanism – increased delocalized cracking – operates in the conch shell. The reduced wet interface cracking stress and presumably $\mathcal{G}_c$, results in an increased amount of cracking between second-, and possibly third-order lamellae. Additional important data still remain to be generated from mechanical testing of shells that are obtained fresh and kept hydrated until testing, thereby preventing the need for artificial reconstitution. Because the natural organic coating on the shells we tested was removed, and because the artificial sea water we prepared was not saturated with respect to $CaCO_3$, it is highly probable that our reconstitution technique resulted in partial dissolution of the shell $CaCO_3$, along the more soluble interfaces. Microscopic examination of a reconstituted test specimen surface did show widened interlamellar spaces, which could, however, be due to an expansion of the organic matrix. In either case, the interfacial cracking observed in the wet specimens may have been artificially enhanced.

4.3.2. Macroscopic layer interfaces

The $\mathcal{G}_c^{delam}$ values obtained for wet and dry delamination cracks are not substantially different from the

values of $\mathcal{G}_c^{chan}$ for wet and dry channel cracks propagating along first-order interfaces. There are no data to support the concept of a different organic structure between the first-order interfaces compared to the macroscopic layer interfaces, and the similarity between the values of $\mathcal{G}_c$ obtained by these two different methods suggests that our estimates of $\mathcal{G}_c$ for the interfaces are valid. Furthermore, it suggests that the fracture strategy embodied by *Strombus gigas* is to use numerous interfaces with the same energy release rate, with the laminate plys arranged to encourage crack arrest, multiple cracking and crack deflection.

It is interesting to note that multiplying $\mathcal{G}_c^{delam}$ by the final area of delamination cracks gives values that are only approximately 5% of the total work of fracture. This indicates that a high toughness is associated with the remaining middle layer, and that the non-linear (frictional and plastic) energy-dissipating mechanisms between the fractured surfaces, contribute a large component of the work of fracture. More importantly, the modest energy dissipation by the interfaces suggests that the interfaces serve a different purpose – that of redistributing the stress away from the catastrophic failure direction.

5. Conclusion

Our work on the fracture of the crossed-lamellar structure suggests that the mechanical advantage of this highly-specialized mollusc shell structure is an increased fracture resistance, in addition to a previously observed increased hardness [1, 8]. From fractographic observations, delocalized damage in the form of multiple channel cracks, crack bridging, crack branching, and delamination cracking occurs, that greatly increases the total crack area and frictional dissipation. During flexural testing of the crossed-lamellar shell, the microcracking events enhance the fracture resistance of dry shell to 4 $kJ\,m^{-2}$, which is 10000 times that of single-crystal aragonite. Reconstituting dry shells by extended soaking in artificial sea water increased the fracture resistance to 13 $kJ\,m^{-2}$, and was correlated to a decreased interfacial strength that resulted in more extensive and closely-spaced cracking patterns.

To understand better the design strategy of the mollusc shell, analyses developed for the fracture of composite laminates were applied to obtain estimates for the fracture resistance of two of the five interfaces present at different length scales. Values of interfacial energy, $\mathcal{G}_c$, for both channel and delamination cracks, were consistently of the order of 100 $J\,m^{-2}$. This suggests that a biomimetic laminate design for high toughness should include layers at several length scales with similar $\mathcal{G}_c$ values to encourage crack branching.

Finite element simulations of multiple channel cracking during bending were conducted, based on a model with a uniform strength of each first-order interface. The qualitative agreement of the strength-based model predictions with the experimental crack-density evolution suggests that the initial channel cracking in crossed-lamellar material may be simply controlled by the strength of the ductile organic interface, in conjunction with the 0°/90°/0° architecture. The numerous interfaces between aragonite grains in the crossed-lamellar structure provide a multitude of sites for energy dissipation, yet allows for non-catastrophic crack initiation and growth. The 0°/90°/0° architecture arrests the easy-to-form channel cracks and encourages additional channel cracking. Channel cracks (between first-order interfaces) that eventually penetrate the middle macroscopic layer are deflected along non-catastrophic $\pm 45°$ second-order lamellar interfaces. It is this complex layered architecture of the crossed-lamellar structure that improves the toughness over that of the nacreous structure. The great number of available sites for crack initiation within the crossed-lamellar structure lead to increased microcracking and energy dissipation.

There are important lessons from such biological ceramic structures that could be readily implemented in the design of tough laminates. The use of laminated *micro*architectures for structural purposes is ubiquitous in Nature – at some level of structure, all structural members made by organisms are laminated, whether or not the structures are mineralized. (Some laminae may be additionally reinforced by fibres.) In the conch shell, there are layers on five size scales, and we have shown that at least three levels of layering were significantly involved in the fracture process (macroscopic layers, first-order layers and second-order layers). Successful exploitation of ceramics in advanced structural applications may be significantly enhanced by the bioinspired use of laminations on at least three size scales, for example, by including a 0°/90°/0° crack-arresting lay-up, combined with $\pm 45°$ sub-layers within those plys to encourage crack deflection. The relatively low *uniform* interfacial fracture energy is also important, as it causes the initial cracking to be delocalized, allowing the exploitation of a wide range of toughening mechanisms. The conch shell is a good example of a whole structural system designed by Nature; likewise, materials engineers should consider designing complete structures and not just materials in isolation.

6. A caveat

The conch shell is apparently designed to a particular strategy: maximization of energy dissipation regardless of the cost in terms of crack formation. This is acceptable as it allows the mollusc to survive the immediate attack of a crab or an impact event in the tidal zone. The mollusc can then hide while it repairs the damaged material. This is similar to the strategy for designing materials for armour, but this design strategy is not necessarily appropriate for structural composites where lifetime and maintenance are also issues.

Acknowledgements

This research was supported in part by a research grant from the Department of Energy administered through Pacific Northwest Laboratory and National

Institutes of Health, National Research Service Award to L. T. Kuhn (now Kuhn-Spearing), administered by Professor Arnold Caplan of the Biology Department, Case Western Reserve University, and a Lynen Fellowship to H. Kessler from the Alexander von Humbolt Foundation (Bonn, Germany). The authors would like to thank Mr C. Tuma for his help with the mechanical testing.

Appendix

We have conducted a simple mechanics analysis to model the evolution of multiple channel cracks extending at least half-way through a laminated beam during four-point bending. The underlying assumption is that the cracks grow from flaws on the tensile surface of the specimen, and that these flaws are initially small compared to the thickness of the layer that is cracking. Given a uniform flaw size, and hence a deterministic material strength, σ_c, the magnitude of the local stress, σ, at the tensile face will determine whether or not fracture will occur at $\sigma \geqslant \sigma_c$. Subsequent crack growth to the simulated inner/middle interface, and across the width of the specimen, will occur at a stress below that to initiate propagation. Such cracking is therefore initiation-controlled.

The finite element method was used to determine the stress fields governing multiple cracking. The code FRANC [24] was chosen because of its convenience for introducing multiple cracks and for subsequent fracture mechanics analysis. The conch shell beam specimens were modelled using eight-noded quadrilateral, isoparametric, plane stress elements. Homogeneous isotropic properties were assumed. Unlike problems of multiple tunnel cracking in tensile loading, it is not possible to assume periodic boundary conditions to simplify analysis, and it is necessary to include several cracks in the model. An array of seven equi-spaced cracks was found to be sufficient, as the stress field and strain energy release rate for the central crack then showed a negligible influence of the outermost cracks. This result indicates that the stress state at this crack was representative of that for any crack in an array with the same density. The remote boundary conditions and applied loads were chosen to give pure bending over the array of cracks, such that no end effects or contact stresses affected the solutions. Solutions for the stresses in both uncracked and single-edge cracked beams were compared with standard solutions [25] to ensure the accuracy of the results; agreement was within 1% for all crack depths considered. Self-consistency was good as solutions for the smallest crack spacings at two different degrees of mesh refinement around the central crack were within 2% for all geometries.

In Fig. A1, the stress, σ, on the tensile surface, mid-way between two existing cracks, is plotted as a function of relative crack spacing, l, for three thickness ratios $h_i/(h - h_i)$. The results are normalized by the stress on the tensile surface, at the same applied load, in the absence of any cracks, σ_0. In order to make use of these finite element solutions, it is useful to fit a simple, empirical mathematical function to the data. Thus the relationship between, σ, l, and $h_i/(h - h_i)$ can be represented by

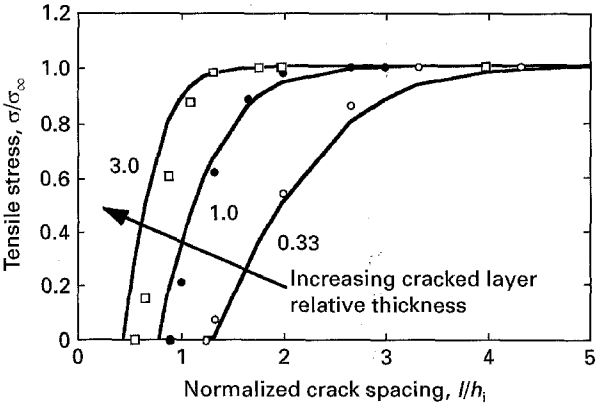

Figure A1 Finite element data for tensile stress midway between two cracks as a function of crack spacing. The empirical fitting function is $\sigma/\sigma_\infty = \tanh\{1.423(l/h_i)[h_i/(h - h_i)]^{1/2} - 1.09\}$.

$$\frac{\sigma}{\sigma_0} = \tanh\left\{1.423\frac{l}{[h_i(h - h_i)]^{1/2}} - 1.09\right\}$$
$$(0.33 < h_i/(h - h_i) < 3) \quad \text{(A1)}$$

This curve fit is shown in Fig. A1.

In order to formulate a model for the manner in which crack density evolves as a function of applied load, the following procedure was used. From beam theory, the stress, σ, is linearly proportional to the applied moment

$$\sigma, \sigma_0 \propto M \quad \text{(A2)}$$

It is also important to note that for a given array of cracks, the problem is linear-elastic. It is convenient to define a bending moment at which the first crack occurs, M_c. This is defined by

$$\sigma_0 = \sigma_c \quad \text{(A3)}$$

At M_c, a characteristic, periodic array of cracks develops, defined by the crack spacing at which the stress first drops below σ_0. In order to create further cracks, it is necessary to increase the applied load, so that the local stress, midway between two existing cracks, is raised, so that

$$\sigma = \sigma_c \quad \text{(A4)}$$

Combining Equations A1–A4, we obtain an expression for the development of cracks according to a criterion of stress-controlled initiation. By working in terms of a normalized load, M/M_c, we avoid having to introduce additional material properties which contribute to M_c, but which have an associated uncertainty of measurement.

Hence

$$\frac{h - h_i}{l} = \frac{1.423[(h - h_i)/h_i]^{1/2}}{[\tanh^{-1}(M_c/M) + 1.09]} \quad \text{(A5)}$$

It should be noted that these expressions are for periodic arrays of equi-spaced cracks, which does not represent the actual situation. The relationship between solutions for periodic and random steady-state cracking is a variant of the "car parking problem"

[26, 27]. The periodic crack density can be converted to an estimate of the random crack density at a given applied load by dividing by a factor of 1.334. This is applied to Equation A5 and the resulting expressions are plotted in Fig. 9b.

There are two important points to note when comparing the predicted crack density evolution with experiment – the predicted sensitivity to relative layer thickness, and the saturation limit to the crack density at higher applied loads. This reflects the complete shielding of the region between cracks at high crack densities, as shown in Fig. A1.

References

1. J. D. TAYLOR and M. LAYMAN, *Palaeontology* **15** (1972) 73.
2. A. J. KOHN, E. R. MEYERS and V. R. MEENAKASHI *Proc. Nat. Acad. Sci.* 76 (1979) 3406.
3. V. J. LARAIA and A. H. HEUER, in "Proceedings of the 11th Risø International Symposium of Metallurgy and Materials Science, edited by J. J. Bentsen, J. B. Bilde-Sørensen, N. Christiansen, A. Horsewell, and B. Ralph (Risø National Laboratory, Denmark, 1990) p. 79.
4. N. V. WILMOT, D. J. BARBER, J. D. TAYLOR and A. L. GRAHAM, *Philos. Trans. R. Soc. Lond. B* **337** (1992) 21.
5. S. WEINER, *Am. Zool.* **24** (1984) 945.
6. J. D. CURREY and A. J. KOHN, *J. Mater. Sci.* **11** (1976) 1615.
7. A.P. JACKSON, J. F. V. VINCENT and R. M. TURNER, *Proc. R Soc Lond. B* **234** (1988) 415.
8. V. J. LARAIA and A. H. HEUER, *J. Am. Ceram. Soc.* **72** (1989) 2177.
9. J. COOK and J. E. GORDON, *Proc. R. Soc. A.* **282** (1964) 508.
10. A. G. EVANS, F. W. ZOK and J. DAVIS, *Compos. Sci. Technol.* **42** (1991) 3.
11. C. A. FOLSOM, F. W. ZOK, F. F. LANGE and D. B. MARSCHALL, *J. Am. Ceram. Soc.* **75** (1992) 2969.
12. W. J. CLEGG, K. KENDALL, N. McN, ALFORD, T. W. BUTTON and J. D. BIRCHALL, *Nature* **347** (1990) 455.
13. M.-Y. HE and J. W. HUTCHINSON, *J. Appl. Mech.* **56** (1989) 270.
14. G. J. VERMEIJ, "A Natural History of Shells" (Princeton University Press, New Jersey, 1993) p. 102.
15. P. G. CHARALAMBIDES, H. C. CAO, J. LUND and A. G. EVANS, *Mech. Mater.* **8** (1990) 269.
16. J. D. CURREY and J. D. TAYLOR, *J. Zool. Lond.* **173** (1974) 395.
17. A. P. JACKSON, J. F. V. VINCENT and R. M. TURNER, *J. Mater. Sci.* **25** (1990) 3173.
18. J. W. HUTCHINSON and Z. SUO, *Adv. Appl. Mech.* **29** (1990) 134.
19. H. G. TATTERSALL and G. TAPPIN, *J. Mater. Sci.* **1** (1966) 296.
20. D. BROEK, "Elementary Fracture Mechanics" (Kluwer Academic, Dordrecht, 1991) p. 123.
21. P. G. CHARALAMBIDES, J. LUND, A. G. EVANS and R. M. McMEEKING, *J. Appl. Mech. (Trans. ASME)* **56** (1989) 77.
22. S. A. WAINWRIGHT, W. D. BIGGS, J. D. CURREY and J. M. GOSLINE, "Mechanical Design of Organisms" (Princeton University Press, Princeton, NJ, 1976) p. 167.
23. S. P. TIMOSHENKO and J. M. GERE, "Mechanics of Materials" (Van Nostrand, New York, 1972) p. 309.
24. P. WAWRZYNEK and A. R. INGRAFFEA, "FRANC 2-D: A Two-dimensional Crack Propagation Simulator" (NASA Contractors Report 4572, Cornell University, 1994).
25. H. TADA, P. C. PARIS and G. R. IRWIN, "The Stress Analysis of Cracks Handbook" (Paris Productions, MO, 1985).
26. A. C. KIMBER and J. G. KEER, *J. Mater. Sci. Lett.* **1** (1982) 353.
27. F. W. ZOK and S. M. SPEARING, *Acta Metall. Mater.* **40** (1992) 2033.

Received 1 May 1995
and accepted 2 July 1996